Journal of Biomedical Materials Research Part B: Applied Biomaterials

WILEY

Society For Biomaterials

RESEARCH ARTICLE

Cytotoxic Impact of Catalytic Activity and Heating Efficiency of Manganese Ferrite Nanoparticles With Different Particle Sizes for Magnetic Fluid Hyperthermia

Marco A. Morales Ovalle[1,2,3] | Mariana Raineri[2,3] | Marcelo Vasquez Mansilla[2,3] | Elin Lilian Winkler[1,2,3] | Roberto Daniel Zysler[1,2,3] | Enio Lima Jr[2,3] | Teobaldo Enrique Torres[1,2,3]

[1]Instituto Balseiro, CNEA-Universidad Nacional de Cuyo, Centro Atómico Bariloche, Rio Negro, Argentina | [2]Instituto de Nanociencia y Nanotecnología, Nodo Bariloche, CNEA-CONICET, Centro Atómico Bariloche, Rio Negro, Argentina | [3]Laboratorio de Resonancias Magnéticas, Gerencia de Física, Centro Atómico Bariloche, Rio Negro, Argentina

Correspondence: Mariana Raineri (marianarainieri@integra.cnea.gob.ar) | Teobaldo Enrique Torres (teo@unizar.es)

Received: 15 January 2025 | **Revised:** 16 July 2025 | **Accepted:** 2 August 2025

Funding: This work was supported by the Argentinean ANPCyT through grants PICT No. 2018-02565, 2019-01859, 2019-02059, and PICT-BCIE 2021-00155. Additional support was provided by the MSCA RISE-2020 101007629-NESTOR project and the CONICET PIBAA No. 28720210100483CO.

Keywords: catalytic activity | cytotoxicity | magnetic hyperthermia | manganese ferrite nanoparticles | specific loss power

ABSTRACT

Magnetic nanoparticles have garnered significant attention in cancer treatment for their dual ability to generate localized heat under an alternating magnetic field and catalyze heterogeneous Fenton-based reactions on their surface. These reactions produce free radicals in mildly acidic and reducing environments, such as the tumor microenvironment, leading to oxidative stress in cancer cells. The synergistic combination of magnetic hyperthermia and catalytic activity enhances oxidative stress induction, underscoring the importance of understanding the cytotoxic effects of this approach. In this study, we performed in vitro toxicity assays on the HepG2 cell line to evaluate cytotoxicity and lipid peroxidation induced by hyperthermia using manganese ferrite nanoparticles with mean sizes of 12 and 28 nm. Magnetic hyperthermia efficiency, quantified by Specific Loss Power (SLP), and catalytic activity, assessed through free radical generation using electron paramagnetic resonance (EPR) and substrate oxidation rates via UV–visible spectroscopy, were characterized prior to the biological experiments. Our results showed that the 28 nm nanoparticles achieved a temperature increase of approximately 11.5°C, compared to 3.6°C for the 12 nm particles. Correspondingly, higher cell death was observed for the 28 nm nanoparticles following magnetic fluid hyperthermia treatment. However, lipid peroxidation was more pronounced with the 12 nm nanoparticles, attributed to their larger surface-to-volume ratio enhancing catalytic performance. In conclusion, nanoparticle size critically influences both magnetic and catalytic properties, and optimizing these parameters is essential for maximizing therapeutic efficacy in magnetic fluid hyperthermia.

1 | Introduction

Magnetic nanoparticles (MNPs) have been widely used for bioseparation, as biosensors, for magnetic resonance imaging, and for magnetic fluid hyperthermia (MFH) for tumor therapy [1–5]. Specifically, MFH has emerged as a promising therapeutic technique for cancer treatment, using the heat generated by the magnetic loss of MNPs under an alternating magnetic field to induce localized hyperthermia in target tissues [6, 7]. Intense efforts have been directed toward designing MNP systems with high specific loss power (SLP) in the intracellular medium, prioritizing magnetic moment inversion against the anisotropy

---

Marco A. Morales Ovalle and Mariana Raineri contributed equally to this work.

energy barrier (Néel relaxation) over mechanical rotation against viscosity [8, 9]. Among the various magnetic nanoparticles utilized in MFH, manganese ferrite nanoparticles with the formula $Mn_xFe_{3-x}O_4$ (MnIONPs) have received significant attention due to their potentially lower anisotropy and higher saturation magnetization in bulk, which is beneficial for effective heat generation in MFH applications [10, 11].

MnIONPs hold significant potential for bio-applications, taking advantage of not only their magnetic properties but also their catalytic activity, particularly in heterogeneous Fenton-based reactions. In the presence of hydrogen peroxide, these nanoparticles generate free radical species, which can induce cell toxicity through oxidative stress, thereby enhancing their therapeutic efficacy within the tumoral tissue [12–14]. Given that heterogeneous Fenton-related activity is due to Fe/Mn at the nanoparticle surface, it is anticipated that smaller MnIONPs, with higher surface to volume, will exhibit higher catalytic activity. This hypothesis has been supported by several studies demonstrating enhanced peroxidase-like activity in smaller nanoparticles [15–17]. The structure, morphology, composition, and surface modifications of MNPs significantly influence their activity [18, 19]. The size of nanoparticles, in particular, plays a crucial role in determining their magnetic and catalytic propeties, since smaller nanoparticles offer a larger surface area for catalytic reactions [15]. Conversely, considering systems with low anisotropy, larger nanoparticles could provide better magnetic heating efficiency but have a reduced surface area, potentially lowering catalytic activity. Understanding these size-dependent effects through in situ experiments is critical for optimizing the design of MNPs for dual functionality in MFH and catalytic applications.

This subject is addressed in this work, where MnIONPs of 12 and 28 nm in particle size were synthesized by high-temperature decomposition of organometallic precursors. The morphology, composition, and magnetic response of these MnIONP systems were characterized by transmission and scanning electron microscopy (TEM and SEM), vibrating-sample magnetometer (VSM), superconducting quantum interference devices (SQUID), ferromagnetic resonance (FMR) and X-ray Photoelectron Spectroscopy (XPS). Their efficiency in MFH experiments was determined by the SLP obtained for experiments performed in hexane, water, and butter oil, thus changing drastically the viscosity of the medium. As-prepared systems are hydrophobic, coated with oleic acid. Thus, oleic acid was removed, and the MnIONPs were functionalized with glucose, which was evidenced by attenuated total reflection Fourier transform infrared spectroscopy (ATR-FTIR). The free radical formation rate from the decomposition of H_2O_2 was assessed by electron paramagnetic resonance (EPR) in uncoated and glucose-functionalized MnIONPs. The peroxidase-like activity of the samples was assessed by UV–visible spectrophotometry with the 2,2′-azino-bis (3-ethylbenzothiazoline-6-sulfonic acid) (ABTS) and 3,3′,5,5′-tetramethylbenzidine (TMB) peroxidase substrate in the presence of H_2O_2, as well.

Finally, size-dependent efficiency of samples in MFH in vitro experiments was evaluated using the HepG2 cell line, which was exposed to an alternating magnetic field (170 Oe, 646 kHz) for 30 min. After treatment, cell viability was determined using the trypan blue exclusion assay, and oxidative stress was assessed through the thiobarbituric acid reactive substances (TBARS) assay.

The results presented in this work aim to contribute to the broader field of nanomedicine and enhance the clinical application of MFH, providing a deeper understanding of the size-dependent effects on the $Mn_xFe_{3-x}O_4$ nanoparticles, and offering valuable insights for the development of optimized MFH treatments by elucidating the relationship between nanoparticle size and catalytic activity for therapeutic efficacy.

2 | Materials and Methods

2.1 | Materials

Chemicals were obtained from the following suppliers: hydrogen peroxide from Anedra; sodium acetate from Biopack; sodium bicarbonate from Cicarelli; disodium hydrogen phosphate, potassium dihydrogen phosphate, sodium chloride, and sodium carbonate from Mallinckrodt Pharmaceuticals Inc.; and acetic acid from Merck Millipore. Additional reagents included 5,5-dimethyl-1-pyrroline N-oxide (DMPO, purity > 97%), DMSO (purity > 99%), ABTS, Trypan blue, anhydrous glucose, and thiobarbituric acid, all sourced from Sigma Aldrich. Cell culture media were obtained from Gibco, Bovine Fetal Serum from Natocor Argentina, and 4-(2-hydroxyethyl)-1-piperazineethanesulfonic acid (HEPES) free acid from Bio Basic. TMB ready-to-use solution was obtained from Ingenasa (Madrid, Spain). Chemical reagents used for nanoparticle synthesis were of pure grade. These included oleic acid (analytical standard), oleylamine (70%), benzyl ether (98%), 1,2-octanediol (98%), Fe(III) acetylacetonate (97%), and Mn(II) acetylacetonate, all acquired from Sigma Aldrich. For the washing procedures, methanol and ethanol of technical grade and acetone meeting the general requirements of the European Pharmacopeia were used. Chloroform (purity > 99%) and toluene (purity 99.8%) were of reagent-plus grade. Hydrochloric acid (HCl, 37%) conformed to the specifications set by the American Chemical Society. In the EPR experiments, quartz tubes with a thickness of 2 mm were utilized. A MgO crystal doped with manganese ions was used as a standard for free radical quantification.

2.2 | Nanoparticle Synthesis

MnIONPs were synthesized via the thermal decomposition of organometallic precursors at high temperatures. The synthesis involved 1 mmol of $Mn(acac)_2$, 2 mmol of $Fe(acac)_3$, 9 mmol of oleic acid, and 3 mmol of oleylamine. The MnIONP_12 nm was prepared by adding 7.5 mmol of 1,2-octanediol to the previously described solution, which was then mixed in 50 mL of benzyl ether in a three-neck flask with mechanical stirring. The system was heated to 120°C under a nitrogen atmosphere and maintained for 30 min to remove humidity. Subsequently, with a glass condenser in place to prevent solvent loss, the system was heated to 200°C and maintained for 60 min. The temperature was then increased to reflux conditions (286°C) and held for 60 min. Finally, the system was cooled to room temperature. The MnIONP_28 nm was synthesized by adding

1.5 mmol of 1,2-octanediol to the base solution, which was mixed in 40 mL of benzyl ether and 10 mL of 1-octadecene. The same process was followed as for the MnIONP_12 nm, with the only modification being an extended time of 75 min at reflux conditions. In both cases, the resulting MnIONPs were washed twice with acetone and ethanol using magnetic assistance, precipitated using a FeNdB permanent magnet, and re-dispersed in hexane.

The final samples consisted of hydrophobic nanoparticles coated with oleic acid. In order to obtain hydrophilic particles, we functionalized the MnIONPs with sterile glucose. For this, an initial exposure to methanol for 8 h was followed by a 48-h incubation in acetone at 40°C. Uncoated particles were obtained by several rounds of washing with methanol and acetone for 72 h. The functionalization with glucose was performed in a sterile hood by incubating 1 g of glucose for every 100 mg of uncoated MnIONPs in ammonia. After 48 h, the MnIONPs were precipitated with the FeNdB permanent magnet to remove the ammonia solution and washed three times in sterile milli-Q water.

2.3 | Nanoparticle Size and Composition Analysis

The size dispersion of the MnIONPs was determined through TEM using a Thermo Fisher Scientific Tecnai F20 microscope operating at 200 kV. TEM specimens were prepared by depositing a solution of MNPs dispersed in hexane onto a copper grid. Size histograms were constructed from measurements of approximately300–500 particles in arbitrarily chosen regions of representative TEM images, and the mean particle size ($\langle d \rangle$) and dispersion (σ) were estimated by fitting the data with a log-normal distribution.

The chemical composition was obtained by energy-dispersive X-ray spectroscopy (EDS) of the MNP powders using scanning electron microscopy (SEM) with a Thermo Fisher Scientific Inspect S50 microscope operating at 30 kV.

2.4 | Determination of MnIONP Concentration

Known volumes of the magnetic fluid were dried in an oven at 100°C and weighed to determine their mass. These particles were then analyzed using thermogravimetric analysis (TGA) using a DTG-60H instrument (Shimadzu) under an argon atmosphere to prevent oxidation, with a flow rate of 100 mL/min. Samples were heated from room temperature to 900°C at a constant heating rate of 2°C/min.

Magnetic characterization of the dried nanoparticles was conducted using a 7307 Lake Shore VSM at room temperature. To determine the magnetization as a function of the magnetic mass, the contribution of the coating to the particle weight was subtracted.

2.5 | Ferromagnetic Resonance Measurements

FMR measurements were performed at 300 K using an ELEXSYS II-E500 spectrometer operated in an X-band resonant cavity (9.4 GHz). For FMR measurements, the samples were prepared by dispersing 0.1 wt% of the MnIONPs in a polymer resin, which was then dried for 8 h under a static magnetic field of 8 kOe within a 2 cm air gap between two permanent magnets (diameter = 8 cm). Subsequently, a smaller section ($0.5 \times 0.2 \times 0.2\ \mathrm{cm}^3$) from the center of the solid resin was extracted and placed in the FMR spectrometer to measure the angular dependence of the resonance field (H_r).

2.6 | Free Radical Production

The generation of DMPO adducts was determined at room temperature using the ELEXSYS II-E500 EPR spectrometer equipped with an X-band resonant cavity (9.4 GHz). The reaction mixtures for the EPR experiments were prepared by dispersing 120 μg of MnIONPs in 200 μL of a 10 mM acetate buffer solution (pH = 5) and 50 μL of a DMPO/water solution ($0.33\ \mathrm{g\,mL^{-1}}$). The reaction was initiated by the addition of 10 μL of 30% H_2O_2 (0.49 M). The solution was contained in a Q-band quartz tube with a diameter of 1 mm. To quantify the amounts of DMPO adducts, the EPR spectrum of each solution was recorded simultaneously with a MgO pattern crystal doped with a known concentration of Mn^{2+} attached to the tube. All spectra were processed using the Spin software from Bruker. The baseline for each spectrum was computed with a 3rd-degree polynomial and then subtracted. After that, the resonance lines were fitted using the hyperfine parameters of the identified components. The concentrations of DMPO adducts were determined by comparing the fitted EPR spectrum intensities of each species with the intensity of the MgO/Mn^{2+} standard.

2.7 | Characterization of Glucose-Functionalized Nanoparticles

After glucose functionalization of MnIONPs, the apparent zeta-potential of the nanoparticle dispersions was measured using a dynamic light scattering (DLS) instrument equipped with a zeta-potential analyzer (Zetasizer 1000, Malvern Instruments). Prior to the measurements, the nanoparticles were suspended at a concentration of 25 μg/mL in 1.5 mM of NaCl prepared in milli-Q water and ultrasonicated for 5 min to ensure uniform dispersion. Measurements were conducted at 25°C ± 1°C in a disposable zeta cell. The Smoluchowski approximation was used for the analysis, and a voltage of 150 mV was applied during the measurements. Each measurement consisted of an average of three runs, with each run containing at least 10 sub-measurements to ensure accuracy and reproducibility. The reported zeta potential values are the mean ± standard deviation of three independent measurements.

To verify the correct functionalization, ATR-FTIR spectra were recorded at a spectral resolution of $4\ \mathrm{cm}^{-1}$ from 500 to $4000\ \mathrm{cm}^{-1}$ with a Spectrum Two spectrometer (PerkinElmer). Each spectrum was averaged over a total of four scans.

Magnetization as a function of temperature was measured using a SQUID magnetometer. The measurements were conducted in both zero-field-cooled (ZFC) and field-cooled (FC) modes, applying a magnetic field of $H = 100$ Oe. For ZFC measurements, the sample was cooled to low temperatures in the absence of an applied magnetic field, and magnetization was recorded during the warming process under a constant applied field. For FC measurements, the sample was cooled under an applied field, and magnetization was recorded during the warming process under the same field conditions. The thermal decay of remanence, denoted as I_r (T), was evaluated by applying a field of $H = 5$ kOe at 5 K to saturate the sample, then reducing the field to zero and subsequently starting to record the remanent magnetization at increasing temperatures. ZFC and I_r (T) measurements were conducted across a temperature range from 10 to 300 K. The irreversibility temperature, defined as the temperature where ZFC and FC curves split, was recorded to characterize the magnetic blocking behavior.

X-ray Photoelectron Spectroscopy (XPS) measurements were performed on powdered glucose-coated MnIONP samples using a Kratos AXIS Supra surface analysis system (Kratos Analytical Ltd., UK). Due to the magnetic nature of the materials, spectra were acquired in electrostatic lens mode without charge neutralization. Survey spectra were recorded with a pass energy of 160 eV, and high-resolution spectra of the Fe 2p and Mn 2p regions were acquired using a pass energy of 20 eV. Peak fitting was conducted using CasaXPS software. After Shirley background subtraction, the peaks were fitted with a mixed Gaussian–Lorentzian line shape.

2.8 | Heating Efficiency Measurements

Magnetic fluid hyperthermia experiments were conducted using a D5 Series nB Nanoscale Biomagnetics magnetic field applicator at frequencies of 571 and 646 kHz and an applied magnetic field amplitude of 170 Oe. The efficiency of the nanoparticles as heating agents was determined by the SLP, calculated using the formula:

$$\mathrm{SPL} = \frac{C\mathrm{Liq} \cdot m\mathrm{Liq} \cdot \Delta T}{m\mathrm{MNPs} \cdot \Delta t}$$

where C_{Liq} is the heat capacity of the liquid carriers, and m_{Liq} and m_{MNPs} are the masses of the liquid and nanoparticles, respectively. Three different media were tested: (a) 0.5 wt% of oleic acid-coated MnIONPs dispersed in hexane [$\eta(295\,\mathrm{K}) = 0.3$ mPa s]; (b) 0.32 wt% of oleic acid-coated MnIONPs dispersed in clarified butter oil [CBO, $\eta(295\,\mathrm{K}) = 477$ mPa s] and (c) 0.6 wt% of glucose-functionalized MnIONPs dispersed in water [$\eta(295\,\mathrm{K}) = 1$ mPa·s]. The CBO samples were prepared by dispersing the required number of MnIONPs in hexane to achieve the final concentration, followed by MnIONPs precipitation with a permanent magnet and the addition of CBO at 313 K.

2.9 | Peroxidase-Like Activity

The intrinsic peroxidase-like activity of the MnIONPs was assessed using a published protocol with an ABTS substrate at room temperature [20], and a previously reported method from our group employing TMB as the peroxidase substrate [21]. The absorbance of the oxidized substrates was measured at 650 nm for TMB and at 420 nm for ABTS using a Shimadzu UV–Visible 1900 spectrophotometer at room temperature.

2.10 | Cell Culture

The HepG2 human hepatocellular carcinoma cell line (ATCC HB-8065) was cultured in high glucose Dulbecco's modified Eagle's medium (Gibco) supplemented with 10% fetal bovine serum (Natocor, Argentina), 100 U/mL penicillin, 100 μg/mL streptomycin, 0.25 μg amphotericin B, and 2 mM L-glutamine (Gibco). The cells were maintained in a saturated humidity atmosphere containing 5% CO_2 at 37°C.

2.11 | Nanoparticle Dose-Dependent Toxicity

A total of 1.7×10^6 HepG2 cells were seeded in a 10 mm cell culture plate (Genbiotech SRL). After 48 h, the cells were incubated with different doses of MnIONPs (0, 100 μg/mL and 200 μg/mL) for an additional 24 h. Following this incubation period, the cells were washed twice with phosphate buffered saline (PBS), detached using 0.05% Trypsin–EDTA (Gibco) for 10 min, centrifuged at 400 g for 5 min, and resuspended in 310 μL of DMEM supplemented with 15 mM of HEPES buffer (pH 7.4). The cell suspension was then divided into three aliquots: 200 μL for MFH treatment, 100 μL maintained in an incubator in a closed tube at 37°C, and 10 μL was used for cell counting using a Luna-II counter (Logos Biosystems). All experiments were performed in triplicate.

2.12 | In Vitro Experiments of MFH

To investigate the effects of MFH treatment on cells, specifically focusing on the thermal responses impacting cell viability, cells were first thermalized at 36.5°C and then exposed to an alternating magnetic field of 170 Oe and 646 kHz for 30 min. Temperature was continuously monitored during and after the magnetic field exposure to ensure that hyperthermia was attributable to the field and not to external thermalization. Following exposure, the cell suspension was mixed at a 1:1 ratio with a 0.4% Trypan Blue solution to assess cell viability using the Trypan Blue exclusion method.

2.13 | Lipid Peroxidation (TBARs)

Lipid peroxidation was analyzed using an adapted version of the TBARS assay as described by Aguilar Diaz De Leon and Borges [22]. Briefly, 30 μL of the cell suspension (including the culture media) obtained after magnetic field exposure was mixed with 100 μL of 8% SDS, 750 μL of 3.5 M acetate buffer (pH 4.0), 750 μL of 0.35% thiobarbituric acid in 20% acetic acid, and 350 μL of Milli-Q water. The samples were then heated in a thermalized shaker (Numak MS-100) for 1 h at 95°C, cooled on ice for 10 min, and centrifuged at 15,000 rpm for 10 min. Absorbance was measured at 532 nm, and malondialdehyde (MDA) concentration was calculated and normalized to the number of cells exposed to the MFH or control treatment (kept at 37°C in the incubator).

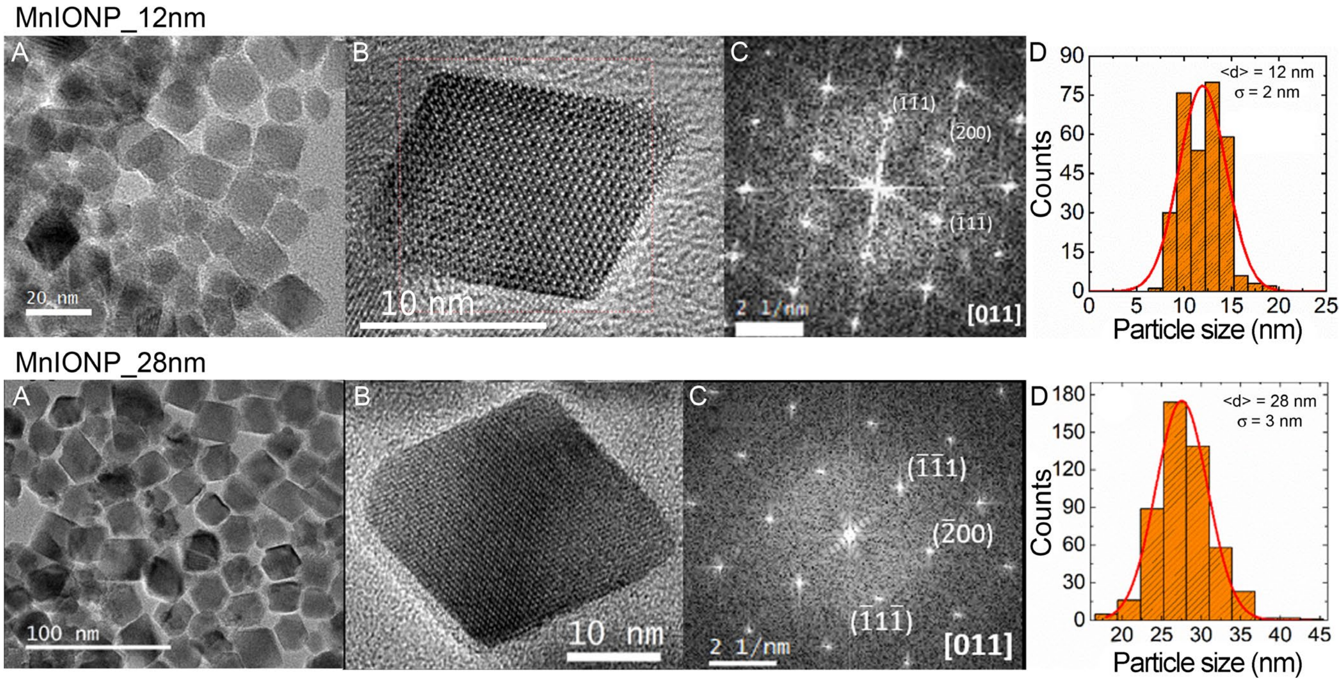

FIGURE 1 | (A) TEM image of the MnIONP_12 nm (upper panel) and MnIONP_28 nm sample (lower panel); (B) HRTEM image of an individual nanoparticle; (C) Fast Fourier transform (FFT) of the HRTEM image; and (D) Size histogram with log-normal fit (solid line).

2.14 | Statistical Analysis

Data were statistically analyzed using R version 4.3.2 (2023). An analysis of variance (ANOVA) followed by Tukey's post hoc test was performed to compare different groups. The Shapiro-Wilk test was used to confirm that the data fit a normal distribution, and Bartlett's test was employed to verify the homogeneity of variances among samples. Differences between groups were considered significant at a p-value of <0.05. Results are presented as mean ± standard deviation.

3 | Results

3.1 | Nanoparticle Characterization

As previously reported for the thermal decomposition synthesis route, the final average particle size and morphology are influenced by various experimental parameters [23, 24]. In this study, two samples with distinct mean particle sizes ($\langle d \rangle$) were prepared. The final control of magnetic nanoparticles' $\langle d \rangle$ was achieved by modifying three parameters: the agitation speed during the synthesis reaction, the reflux time, and the molar ratio between the precursors (acetylacetonates) and 1,2-octanediol (see Experimental section for details). Analysis of representative TEM images evidenced that the two synthesized MnIONPs present uniform size and a faceted octahedral shape (Figure 1A,B), indicative of a high crystallinity degree in both samples. The size distribution of the nanoparticles was determined by approximating their shape as spherical and fitting the data to a log-normal distribution for both samples. This analysis yielded mean particle sizes of $\langle d \rangle = 12$ and 28 nm with standard deviations (σ) of 2 and 3 nm, respectively (Figure 1D). Moreover, as can be observed in the HRTEM images (Figure 1C), both samples confirm the high crystallinity degree and the cubic crystalline structure through the indexation of the fast Fourier transform (FFT) in the [011] zone axis, corresponding to the (1¯ 1¯ 1), (2¯20), and (1¯ 11¯) planes.

In order to determine the relative concentration of Mn and Fe in the samples, we performed compositional EDS during SEM and TEM measurements in three areas from different locations of the samples to acquire the corresponding spectra (Figure S1). The differences in the results obtained for the composition of these zones were consistent within the experimental error, confirming the macroscopically homogeneous nature of the samples (Table S1). Nevertheless, concerning the global composition of the sample, a deviation from nominal stoichiometry incorporated in the synthesis solution ($[\mathrm{Fe}]/[\mathrm{Mn}] = 2$) was observed. The composition obtained for the samples, assuming the general formula $\mathrm{Mn}_x\mathrm{Fe}_{3-x}\mathrm{O}_4$ expected for Mn-incorporated ferrites, was determined to be $x = 0.5$ and 0.6 for the MnIONPs with particle sizes of 12 and 28 nm, respectively (Table 1).

For nanoparticle concentration determination, hysteresis loop measurements at $T = 5$ K yielded a magnetic saturation value (M_S) of 77 emu/g for both samples. At room temperature, M_S decreased to 66 emu/g for the 12 nm nanoparticles and 61 emu/g for the 28 nm nanoparticles (Figure S2, left panel). The oleic acid content of the MnIONPs was determined by TGA analysis, as shown in the right panel of Figure S2. The thermal decomposition profile of the oleic acid-coated MnIONPs was consistent with the typical curves reported for oleic acid-coated iron oxide nanoparticles under an inert atmosphere [25, 26].

The effective magnetic anisotropy can be estimated from the anisotropy field, $H_A \sim 2K_e/M_S$, obtained from FMR by analyzing the angular dependence of the resonance field (H_R) in oriented samples (Figure S3) [27]. Based on these measurements, we

TABLE 1 | Parameters obtained from TEM and SEM analysis of MnIONP samples.

Parameter		MnIONP 12 nm	MnIONP 28 nm
Size (nm)		12 ± 2	28 ± 3
Formula	$Mn_xFe_{3-x}O_4$	$Mn_{0.50}Fe_{2.50}O_4$	$Mn_{0.62}Fe_{2.38}O_4$
[Fe] / [Mn]	EDS-SEM	5.03 ± 0.03	3.90 ± 0.03
	EDS-TEM	5.87 ± 0.04	3.56 ± 0.79

TABLE 2 | Parameters obtained at low and high temperatures.

Parameter	T (K)	MnIONP 12 nm	MnIONP 28 nm
H_C (Oe)	5	370	395
	300	6	56
M_S (emu/g)	5	77	77
	300	66	61
$K_e \times 10^5$ (erg/cm^3)	—	1.30	0.25

Note: Effective magnetic anisotropy constant (K_e) derived from the fitting of I_r (T) data.

TABLE 3 | Parameters obtained from EPR and SLP calculation for MnIONP samples in different solvent.

Parameter	Time (min)	MnIONP 12 nm	MnIONP 28 nm
[DMPO/OH] (nM)	10	2335 ± 233	1211 ± 121
	40	2095 ± 210	917 ± 92
SLP (W/g)	Hexane	59	551
	CBO	44	90
	Water	37	92

obtained H_A values of 0.3 and 0.6 kOe for the MnIONP_12 nm and MnIONP_12 nm samples, respectively. However, it is important to note that this method yields reliable results only for well-oriented systems. In our case, the linewidth exhibits anisotropic broadening, which prevents an accurate determination of the anisotropy. This behavior is particularly evident in the smaller MnIONP_12 nm nanoparticles, which display a broader linewidth of 1.8 kOe compared to 0.9 kOe for MnIONP_28 nm. This broader linewidth suggests the enhanced thermal fluctuation in the smaller nanoparticles hinders their alignment with the magnetic field. Therefore, we estimate the effective anisotropy constant from magnetization measurements, as shown in Table 2.

3.2 | Free Radical Production

The free radical production of both samples was measured through EPR at room temperature using the spin-trap DMPO in 10 mM acetate buffer at pH = 5. This method was employed to detect and identify the reactive oxygen species (ROS) formed by the reaction of the MnIONPs with H_2O_2. As detailed in our previous work, the EPR spectrum comprised the convolution of resonance signals of the different paramagnetic species produced [21, 28] The distinct paramagnetic species can be well characterized by the g-factor (g), hyperfine splitting factor (HSF), and linewidth (w) parameters, as shown in Table S2, which remain unchanged across different experimental conditions for all samples.

For the EPR measurements, the nanoparticles were chemically etched to remove the hydrophobic coating. Since modifications in Fe or Mn typically lead to distinct anisotropy fields—an effect not observed in the FMR measurements performed on the solution containing the etched particles—we assume that no changes in the oxidation state occurred. Quantification of the free radicals was carried out by comparing the intensity signals of each radical's contributions to the Mn^{2+} pattern sample. The DMPO/$^{\bullet}$OH concentration measured for sample MnIONP_12 nm is twice that of sample MnIONP_28 nm (Table 3).

Figure 2 shows the EPR spectra obtained after 10 min of reaction for both samples (along with the corresponding fittings) demonstrating excellent agreement between the experimental data and fitted values. From the fitting, different species were identified as: (i) outer lines corresponding to the central resonance lines of Mn^{2+} ions in the MgO crystal used as a pattern sample; [28] (ii) the DMPO/$^{\bullet}$OH free-radical spectrum, composed of four resonance lines with a 1:2:2:1 intensity ratio due to the hyperfine interaction of the electronic spin with the nuclear spin of nitrogen and hydrogen ions; (iii) three broader lines related to the interaction of the electron spin of oxidized DMPO with a nitrogen ion (DMPO/$^{\bullet}$N); and (iv) the absence of lines associated with hydroperoxyl/superoxide radicals (DMPO/$^{\bullet}$OOH), indicating that these species were not present under the experimental conditions.

3.3 | Characterization of Glucose-Functionalized Nanoparticles

For biological experiments, glucose-functionalized MnIONPs were used. The zeta potential of the nanoparticles was measured (Figure S4), yielding values of -27.5 ± 0.7 mV (-2.161 ± 0.054 μm·cm/V·s) for MnIONP_12 nm and -30 ± 1.6 mV (-2.355 ± 0.128 μm·cm/V·s) for MnIONP_28 nm at a conductivity of 0.2 mS/cm, indicative of moderately or near highly stable dispersion due to electrostatic repulsive

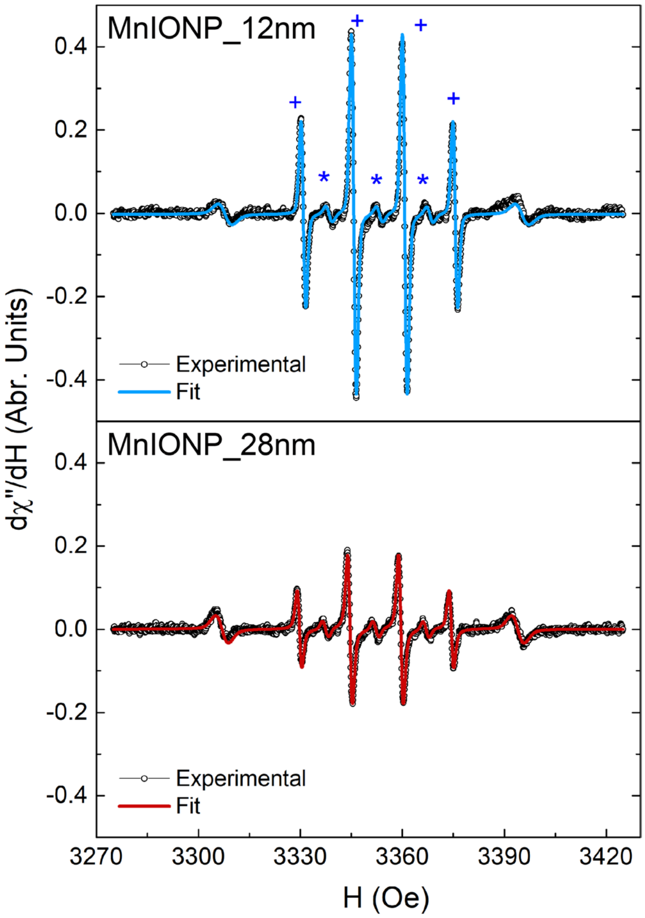

FIGURE 2 | EPR spectrum and corresponding fitting for the uncoated MnIONP_12 nm (upper panel) and MnIONP_28 nm (lower panel), measured 10 min after the addition of H_2O_2 at room temperature in acetate buffer at pH = 5. The (+) symbols indicate the characteristic peaks of DMPO/$^\bullet$OH radical adducts, while the (*) symbols indicate DMPO/$^\bullet$N radical adducts, which were not considered in the discussion.

forces [29]. The ATR-FTIR spectra shown in Figure S5 of the glucose-coated MnIONPs show the disappearance of characteristic oleic acid peaks in the FTIR spectrum: the asymmetric CH_2 vibration at ~2920 cm^{-1}, the symmetric CH_2 stretching at ~2850 cm^{-1}, and the COO− peaks at 1530–1550 and ~1400 cm^{-1} belonging to the symmetric and asymmetric stretching vibrations of the molecule [30]. In addition, the glucose coating results in the presence of a broad peak, probably a composite one, between750 and 1000 cm^{-1}. The vibrational band of Fe–O was observed at 550 and 560 cm^{-1} for the oleic acid-coated MnIONPs of 12 and 28 nm, respectively. Glucose functionalization caused a 6 cm^{-1} shift toward higher wavelength values in both samples, probably due to changes in the local chemical environment.

Magnetization as a function of temperature was recorded in ZFC-FC modes under an applied magnetic field of $H = 100$ Oe. Additionally, I_r (T) was recorded following the application of a 5 kOe field, as shown in Figure S6. For the MnIONP_12 nm sample, the ZFC exhibited a broad maximum below 300 K and the I_r (T) curve shows that the irreversibility disappears at about 150 K. Meanwhile, for 28 nm particles, the system remained blocked across the entire temperature range, indicating an irreversibility temperature above room temperature. Besides, the FC curves of both systems decrease with decreasing temperature, which is a signature of the presence of interparticle interactions. These features result in varying remanent behavior depending on the measurement protocol. In this context, we followed the procedure reported by O'Grady et al. to estimate the effective magnetic anisotropy from the I_r (T) curve [31]. In systems of non-interacting nanoparticles with uniaxial anisotropy and easy axes aligned parallel to the magnetic field, the magnetic anisotropy constant (K_e) can be determined by fitting the I_r (T) according to the expression reported by O'Grady:

$$I_r = I_r(0)\left[1 - \int_0^{Vo} f(\mathrm{V})dV\right]$$

where I_r is the remanence at temperature T, I_r (0) is the remanence at low temperature, $f(V)$ is the volume distribution function of the nanoparticles, and V_o is the critical volume above which the particles remain magnetically blocked at a given temperature. The blocking condition is defined by the relation $KV = 25k_BT_B$, where V is the particle volume, k_B is the Boltzmann constant, and T_B is the blocking temperature. However, when these assumptions are not fulfilled, the fitting becomes unsatisfactory. In such cases, O'Grady et al. [31] proposed an alternative method to estimate an effective magnetic anisotropy, based on the mean particle size and the temperature at which the remanent magnetization decreases to half of its maximum value at low temperature. Applying this approach, we estimated K_e values of 1.3×10^5 erg/cm^3 for the MnIONP_12 nm sample and 0.25×10^5 erg/cm^3 for the MnIONP_28 nm nanoparticles system. These values are in agreement with previous findings, which show that smaller nanoparticles exhibit higher magnetic anisotropy due to enhanced contributions from surface anisotropy [32–35].

XPS was performed on the glucose-functionalized MnIONP nanoparticles to assess their surface composition and oxidation states (Figure S7). The high-resolution spectra of the Mn 2p and Fe 2p regions revealed the coexistence of Mn(II)/Mn(III) and Fe(II)/Fe(III) in both samples, confirming the preservation of the mixed-valence spinel structure after surface modification. The total Mn content at the surface was comparable between the two samples (~33% in MnIONP_12 nm and ~39% in MnIONP_28 nm), with a slightly higher proportion of Mn(III) observed in MnIONP_28 nm, as shown in Table S3.

3.4 | Heating Efficiency Measurements

The heating efficiency of the samples was estimated through SLP measurements. The SLP is one of the most important parameters in MFH treatments because it quantifies the efficiency with which magnetic nanoparticles convert magnetic losses into heat. This parameter is crucial for achieving the desired therapeutic temperature range to effectively target and destroy cancer cells [5, 36].

The SLP of the MnIONP samples was determined under an alternating magnetic field with an amplitude of 170 Oe

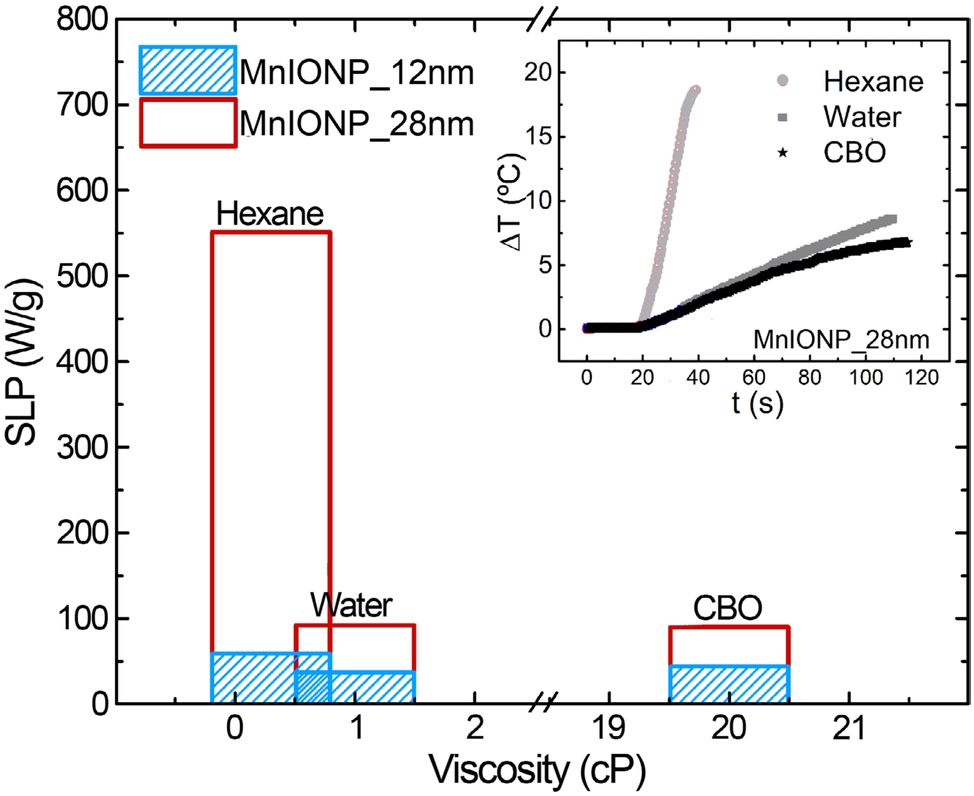

FIGURE 3 | Specific loss power (SLP) as a function of the viscosity of different liquid carriers for the MnIONP_12 nm and MnIONP_28 nm samples. The inset illustrates the temperature change (in °C) over time (in seconds) for the MnIONP_28 nm sample.

(13.5 kA/m) and a frequency of 646 kHz. This parameter quantifies the heat generated by nanoparticles due to energy dissipation via Néel and Brownian relaxation mechanisms, which are influenced by the surrounding medium's viscosity and the particle's magnetic properties. To investigate the interplay between these mechanisms, the SLP was measured in three distinct media with varying viscosities: hexane (low-viscosity), water (intermediate-viscosity), and clarified butter oil (CBO) (high-viscosity). Considering that MNPs in the colloidal state can rotate relatively freely in low-viscosity liquids, such as hexane [10], these conditions offer valuable insights into the relative contributions of Néel and Brownian relaxation mechanisms to the thermal response of MNPs, as shown in Figure 3.

In the case of the MnIONP_28 nm sample dispersed in hexane, the SLP value greatly exceeds that of CBO, indicating that Brownian relaxation is dominant. This does not happen in water, where the SLP is similar to that of CBO, and Néel relaxation is the only possible mechanism. This effect may be attributed to the formation of aggregates during the oleic acid removal process, which hinders Brownian relaxation [37, 38].

Regarding the MnIONP_12 nm sample, the SLP values remain almost constant between37 and 44 W/g. Its smaller size reduces both relaxation times, but that of Néel more than Brownian. As a result, the Néel mechanism prevails regardless of the medium; however, its relaxation time is not tuned with the working MFH, and the SLP is not optimized in this case. For instance, recent reports have shown SLP values up to 700 W/g for $MnFe_2O_4$ nanoparticles with $\langle d \rangle = 46$ nm, dispersed in water, under an alternating magnetic field with an intensity of $H = 300$ Oe (24 kA/m) and $f = 571$ kHz [10]. In comparison, the value of approximately 100 W/g for the 28 nm nanoparticles might seem lower, but they are half the size and measurements were performed with a 30% lower intensity compared to the reported values (the power of the applied field scales with H^2).

3.5 | Peroxidase-Like Activity

To evaluate the peroxidase-like activity of the samples, an ABTS colorimetric assay was performed according to a reported standardized method [20] as shown in Figure 4. Consistent with previous reports on iron oxide nanoparticles, the oxidation of ABTS over time is higher for the 12 nm nanoparticles, indicating greater catalytic activity [39]. The specific activity (SA) of the MnIONPs was calculated, as shown in Table 4, demonstrating that manganese MNPs possess peroxidase-like activity even in the absence of H_2O_2 at acidic pH. This activity increases by approximately 50% with the addition of H_2O_2. Both activities appear to depend on the particle size and were also verified for the TMB substrate (Figure S8).

Quantification of DMPO adducts using EPR (Table S4) reveals that only hydroxyl radicals are observed when nanoparticles are incubated with H_2O_2 at acidic pH. The concentrations of hydroxyl radicals were 337 nM for the 12 nm MnIONPs and 230 nM for the 28 nm MnIONPs, respectively. Furthermore, no hydroperoxyl radical formation was detected.

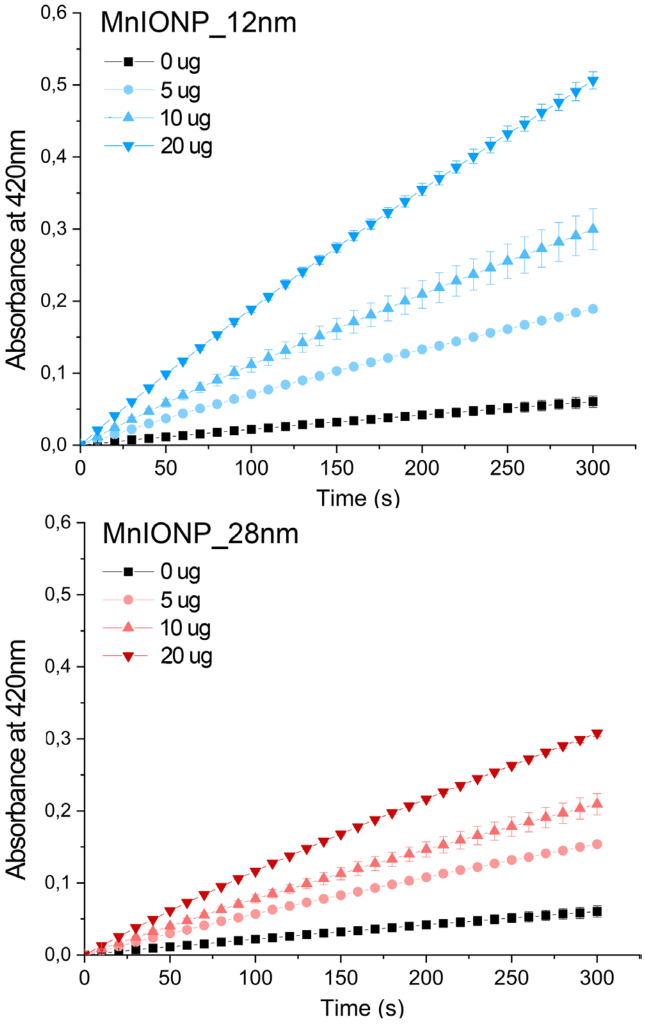

FIGURE 4 | Peroxidase-like activity of the glucose-functionalized MnIONP_12 nm (upper panel) and MnIONP_28 nm (lower panel) samples. Absorbance of ABTS at 420 nm was measured over time for nanoparticle amounts of 5, 10, and 20 µg. Data are expressed as mean ± standard deviation of duplicate measurements.

TABLE 4 | Specific activity (SA) and correlation coefficient (R^2) of the MnIONP samples with and without the addition of 1 M H_2O_2.

	w/o H_2O_2		H_2O_2 1 M	
Sample	**SA (mU/mg)**	**R^2**	**SA (mU/mg)**	**R^2**
MnIONP_12 nm	1.28	0.99	2.36	0.99
MnIONP_28 nm	0.84	0.94	1.33	0.98

Note: SA is measured in mU/mg.

3.6 | Nanoparticle Dose-Dependent Toxicity

Since nanoparticle toxicity can be influenced by the peroxidase-like activity of MnIONPs, we initially aimed to establish the viability of HepG2 cells after 24 h of incubation with different doses of nanoparticles (0–200 µg/mL). As shown in Figure 5, the MnIONPs with 12 nm were more toxic than those with 28 nm, as evidenced by the lower viability observed for this group.

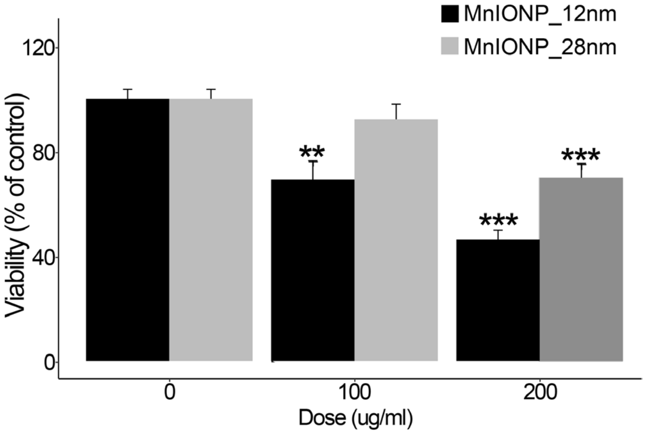

FIGURE 5 | Viability of HepG2 cells after 24 h of incubation with MnIONP_12 nm and MnIONP_28 nm nanoparticles at concentrations of 0, 100, and 200 µg/mL. Data were analyzed using two-way ANOVA followed by Tukey's test. Results are presented as mean ± standard deviation ($n = 3$) as a percentage of the control group Statistical significance is indicated as follows: $^*p < 0.05$, $^{**}p < 0.01$, and $^{***}p < 0.001$.

A two-way ANOVA analysis revealed a significant main effect of nanoparticle type [$F(1, 31) = 11.09$, $p = 0.0021$] and a significant main effect of concentration [$F(2, 31) = 40.13$, $p < 0.001$]. Additionally, there was a significant interaction between nanoparticle type and concentration [$F(2, 31) = 4.16$, $p = 0.025$].

Post hoc comparisons using Tukey's test indicated that the viability of cells treated with MnIONP_12 nm at 100 µg/mL was significantly lower than those treated without nanoparticles ($p = 0.0013$). At the 200 µg/mL concentration, both nanoparticle types reduced viability compared to the control ($p < 0.001$). The 100 µg/mL dose was then chosen to perform the biological experiments.

3.7 | In Vitro Experiments of MFH

The MFH experiment was performed for both samples. To achieve this, HepG2 cell pellets containing the nanoparticles were exposed to an external alternating magnetic field of 170 Oe and 646 kHz for 30 min. The selected parameters for the magnetic field (170 Oe and 646 kHz; $H \times f = 8.74 \times 10^9$ A/m·s^{-1}) are considered to be below the safety limits proposed by Herrero de la Parte et al. in 2022 (9.59×10^9 A/m·s^{-1}), demonstrating no significant biological effects at these frequencies and field strengths [40].

Figure 6 shows the temperature variations for all three groups (without nanoparticles, with MnIONP_12 nm, and with MnIONP_28 nm) over the course of the experiment. The increment in the temperature for the MnIONP_28 nm was significant, with the temperature rising from 36.3°C to approximately 47.8°C (11.5°C). In comparison, the MnIONP_12 nm induced a more modest temperature increase from 36.5°C to 40.2°C (3.7°C). The control group, which did not contain any nanoparticles, exhibited only a slight temperature increase from 36.1°C to 38.3°C, a rise of approximately 2.2°C. This temperature increment might be attributed to current circulating in the coil when applying the magnetic field, and it is expected to affect all measurements equally.

After the MFH experiment, we fixed the cells and performed magnetization measurements to determine the amount of nanoparticles present in the tubes at the time of the experiment. Our analysis using one-way ANOVA revealed no significant differences in nanoparticle content [$F(1, 4) = 0.68$, $p = 0.46$] between the nanoparticle content per tube for the MnIONP_28 nm (286 µg) and the MnIONP_12 nm group (222 µg). These results indicate that the observed temperature increase was not due to variations in nanoparticle concentration.

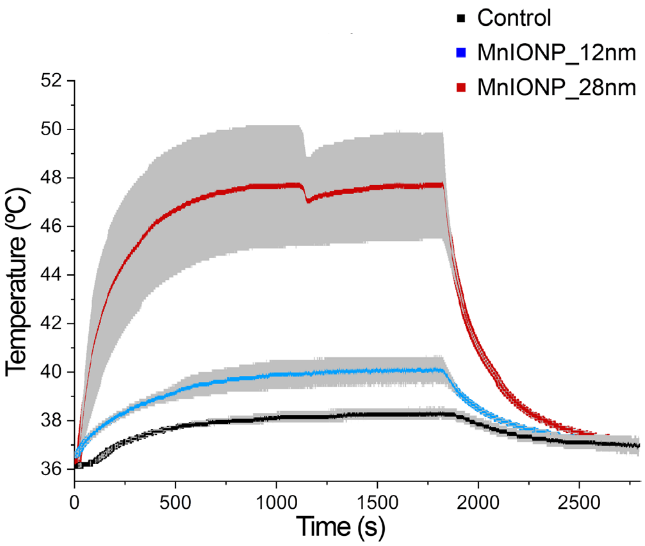

FIGURE 6 | Temperature variations over time in HepG2 cell pellets with glucose-coated MnIONP_28 nm (100 µg/mL), MnIONP_12 nm (100 µg/mL), and the control group without nanoparticles.

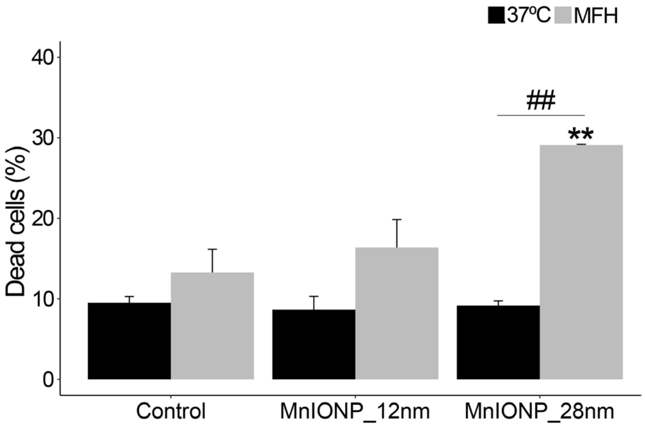

FIGURE 7 | Percentage of dead cells after MFH treatment, as determined by a trypan blue assay. A two-way ANOVA followed by Tukey's post hoc test was performed. * indicates $p < 0.05$, **indicates $p < 0.01$, and ***indicates $p < 0.001$ relative to the control group exposed to the same MFH/incubator treatment. # indicates $p < 0.05$ relative to the same MnIONP treatment group.

3.8 | Hyperthermia-Dependent Toxicity

Immediately following MFH treatment, a trypan blue assay was performed to evaluate the number of cells that died during the MFH treatment. As shown in Figure 7, there was a significant increase in the percentage of dead cells in the MnIONP_28 nm-treated group compared to the control group also exposed to the alternating magnetic field (two-way ANOVA, $p < 0.01$, followed by Tukey's post hoc test).

Additionally, the MFH-treated MnIONP_28 nm group displayed significant differences compared to the MnIONP_28 nm group kept in the incubator at 37°C (two-way ANOVA, $p = 0.001$, followed by Tukey's post hoc test). These findings indicate that the MFH treatment with MnIONP_28 nm nanoparticles significantly enhances cell death relative to both control conditions.

3.9 | Lipid Peroxidation (TBARs)

Finally, it is well established that oxidative stress occurs when free radical production exceeds the cellular antioxidant capacity. One consequence of oxidative stress is lipid peroxidation, which can be measured using the TBARS assay. To evaluate the impact of MFH treatment on free radical production, the TBARS levels were measured in the cell fractions exposed to the alternating magnetic field and in those kept in the incubator. The TBARS assay was conducted to compare the effects of temperature versus MnIONP size (as well as the control group), and it is shown in Figure 8.

The two-way ANOVA analysis [$F_{\mathrm{MFH}}(8, 2) = 93.2$, $p < 0.001$; $F_{\mathrm{MnIONP}}(8, 1) = 28.6$, $p < 0.001$; $F_{\mathrm{MFH \times MnIONP}}(8, 2) = 5.3$, $p < 0.05$], followed by Tukey's post hoc test, revealed a significant difference in the TBARS levels between the MFH treated and incubator group for the MnIONP_12 nm ($p < 0.05$). However, no

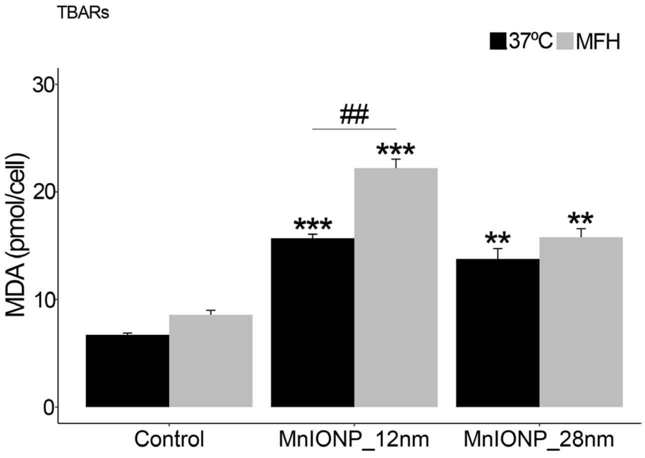

FIGURE 8 | Lipid peroxidation expressed as MDA concentration (pmol/cell) as a function offield exposure, assessed using the TBARS assay. Data are shown as MDA concentration ± standard deviation. The data were analyzed using a two-way ANOVA followed by Tukey's post hoc test. * indicates $p < 0.05$, **indicates $p < 0.01$, and ***indicates $p < 0.001$ relative to the control group exposed to the same MFH/incubator treatment. # indicates $p < 0.05$ relative to the same MnIONP treatment group.

significant differences were found between the MFH and incubator conditions for the MnIONPs with 28 nm. In addition, both samples presented significant differences in comparison to the control group for both conditions: in the incubator and MFH treatment.

4 | Discussion

The results presented provide a comprehensive understanding of the properties and potential applications of Mn-doped iron oxide nanoparticles and underscore the critical interplay between particle size, composition, and functionalization.

The compositional analysis revealed that the relatively low incorporation of Mn ions in the final phase (approximately 50% and 60% of the original nominal value $x = 1$) can be attributed to the formation of weaker magnetic species with higher manganese content that are likely removed during the magnetically assisted precipitation and washing processes [41]. The lower incorporation of Mn compared to Fe ions may be attributed to the delayed onset of decomposition of $Mn(acac)_2$ during the synthesis, which occurs at approximately 246°C, compared to $Fe(acac)_3$, which decomposes around 220°C. This temperature difference likely leads to a reduced availability of Mn^{2+} ions during the critical nucleation and growth stages of the reaction, thereby limiting their substitution for Fe ions in the spinel structure [42, 43]. Nevertheless, no appreciable effect was observed in the structural properties of the samples with the small differences in the composition. The reduction in magnetization values (M_S) at room temperature, by 18% and 24% compared to the bulk phase, reflects the good crystallinity of the samples as observed by TEM analysis. These results align the with expected behavior of nanostructured materials, where surface and finite-size effects significantly influence magnetic properties [44]. These results confirm that the thermal decomposition route used in this study is robust for controlling the size and composition of MnIONPs.

The analysis of the magnetic anisotropy field (H_K) and effective magnetic anisotropy constants (K_e) of MnIONPs provides key insights into the influence of particle size and shape on their magnetic properties. The estimated K_e and H_C values are consistent with those previously reported for $MnFe_2O_4$ nanoparticles of comparable size [32–35] At room temperature, the pronounced reduction in H_c to near-zero values highlights the superparamagnetic behavior of the nanoparticles. This behavior is less evident in the MnIONP_28 nm sample, where a non-negligible fraction of particles—estimated to be approximately 20% based on remanence—remains magnetically blocked at room temperature. In contrast, the MnIONP_12 nm sample exhibits minimal remanence under the same conditions, suggesting it would be more suitable for MFH applications where preventing particle aggregation is essential.

Regarding free radical production, the catalytic behavior of MnIONPs can be explained by heterogeneous Fenton-like reaction mechanisms. In these processes, reactive oxygen species, mainly hydroxyl radicals ($^{\bullet}OH$), are produced through the reaction of H_2O_2 with iron or manganese [45, 46]. As mentioned previously, the reaction depends on the temperature, the size, the structure/morphology (including dopants), and surface modifications of the MNPs [17, 19, 39, 47]. Since both samples exhibited similar morphology and Mn content, and both measurements were performed at the same temperature, we attributed the factor of 2 in the detected $^{\bullet}OH$ concentration to the MnIONP size.

The glucose functionalization of MnIONPs resulted in stable dispersions in water, as evidenced by the zeta-potential values. The absence of oleic acid peaks in the FTIR spectra, along with the observed 6 cm^{-1} shift in the Fe-O vibrational band, can be attributed to changes in the local chemical environment induced by glucose, further confirming successful surface modification [30]. The magnetic characterization revealed significant differences in blocking temperatures between the 12 nm and 28 nm MnIONPs, suggesting size-dependent magnetic behavior. The broader blocking temperature distributions and lower maximum values observed in the $I_r(T)$ curves suggest that there is not a direct association between blocking temperature and particle size distributions [10]. These results indicate that, in addition to particle size, dipolar magnetic interactions play a significant role in shaping the magnetic behavior of the system, with important implications for their potential biomedical applications. This result indicates that particle size significantly influences the magnetic properties and their potential applications in biomedicine.

The comparison of particle SLP performance in hexane (allowing free rotation) and CBO (restricting mobility) confirmed the dominance of the Néel relaxation mechanism in 12 nm MnIONPs, emphasizing the critical role of particle size in relaxation dynamics. Larger 28 nm MnIONPs exhibited superior heating efficiency, attributable to their larger magnetic core size and relaxation time optimized for the applied magnetic field frequency. Enhanced SLP values across all tested solvents corroborate this observation, reinforcing the importance of particle size optimization for MFH applications. A detailed study by de Almeida et al. (2020) supports these findings, emphasizing temperature-dependent thermal properties, including heat capacity (C_p), in calculating SLP values [48].

Catalytic activity assays further revealed that 12 nm MnIONPs exhibit superior peroxidase-like activity, evidenced by a higher ABTS oxidation rate compared to their 28 nm counterparts. This observation aligns with previous reports on iron oxide nanoparticles [39].

On the other hand, direct oxidation of ABTS was observed even in the absence of H_2O_2, although no formation of DMPO adducts was detected by EPR. This unique catalytic behavior of MnIONPs is likely attributable to the presence of manganese, which enables oxidase-like activity independent of ROS. This finding differentiates MnIONPs from Fe_3O_4 nanoparticles, where manganese appears to enhance direct interactions with ABTS or TMB molecules [49]. Furthermore, the dual enzyme-like activities of $MnFe_2O_4$ MNPs highlight the role of the transition metal valence and site occupancy within the spinel structure, as highlighted in prior studies [14, 50, 51].

Given that the suitability of MnIONP_12 nm particles for free radical-based oncological treatments arises from their higher catalytic activity, while MnIONP_28 nm particles are more appropriate for magnetic hyperthermia due to their superior SLP values, hyperthermia experiments were conducted using HepG2 cultured cells.

The observed dose-dependent toxicity of MnIONPs indicates a clear relationship between nanoparticle size and cellular response. Smaller nanoparticles (12 nm) exhibited greater toxicity than their larger counterparts (28 nm), which can be attributed to their higher catalytic activity, as previously evidenced. The two-way ANOVA analysis further highlighted the significant interaction between nanoparticle size and concentration, demonstrating that both parameters significantly influence cell viability.

The decision to use the 100 μg/mL dose for MFH experiments was due to its intermediate toxicity level, enabling biological experiments to proceed without excessively compromising cell viability, while still providing a clear indication of nanoparticle impact. The significant temperature increment observed with MnIONP_28 nm aligns with its higher SLP values, reinforcing the potential efficacy of larger particles in MFH applications. Conversely, the lower temperature increase observed with MnIONP_12 nm highlights the dependence of heating efficiency on nanoparticle size, as larger particles likely exhibit enhanced magnetic response under an alternating magnetic field. Importantly, the absence of significant differences in nanoparticle content between MnIONP_28 nm and MnIONP_12 nm confirms that the observed temperature variations were not attributable to nanoparticle concentration but rather to particle size. The slight temperature rise observed in the control group can be attributed to Joule heating caused by current circulation in the coil during the application of the magnetic field, underscoring the importance of including control groups to account for non-specific heating effects.

With respect to cell viability after MFH treatment, the group treated with MnIONP_28 nm, but not MnIONP_12 nm, showed statistically significant differences compared to the control cells exposed to the alternating magnetic field (without nanoparticles) and the corresponding group maintained in the incubator at 37°C. This can be attributed to the thermal effects associated with hyperthermia: tissue temperatures exceeding 41°C trigger the heat shock protein response, while temperatures in the range of 42°C–46°C cause irreversible damage, with necrosis beginning after approximately 10 min. At temperatures above 60°C, cell death occurs almost instantaneously [52]. In this study, the MnIONP_28 nm sample sustained cell temperatures above 42°C for 30 min, indicating that significant cell death occurred under these conditions.

Finally, since lipid peroxidation is a consequence of oxidative stress caused by an imbalance between increased ROS levels and the antioxidant capacity of the cells [53], we performed a TBARs assay to determine whether MFH exacerbates the catalytic activity of MnIONPs. The results indicate that MFH had a distinct effect on oxidative stress, particularly for the 12 nm MnIONPs. While the smaller nanoparticles induced significant oxidative stress compared to the control, the larger nanoparticles caused higher overall cell toxicity, likely due to the elevated temperatures achieved during the treatment. Ultimately, these findings suggest that in magnetic hyperthermia treatments, the temperature to which cells are exposed appears to be more critical than the catalytic activity of the nanoparticles.

5 | Conclusions

This study provides a detailed investigation into the size-dependent properties and biomedical potential of MnIONPs, highlighting the intricate interplay between particle size, magnetic behavior, and catalytic activity. The compositional and structural analyses confirm the robustness of the thermal decomposition method for synthesizing MnIONPs with controlled size and composition. Despite minor differences in composition, the nanoparticles demonstrated excellent crystallinity, with surface and finite-size effects playing a significant role in their magnetic properties.

Magnetic characterization revealed size-dependent anisotropy and relaxation dynamics, with smaller nanoparticles (12 nm) exhibiting Néel-dominated relaxation and enhanced catalytic activity, while larger particles (28 nm) demonstrated superior heating efficiency in MFH due to their higher SLP. These findings underscore the importance of optimizing nanoparticle size for specific applications, where smaller particles are better suited for free radical-based treatments, and larger ones excel in hyperthermia-based therapies.

Catalytic activity assays highlighted the peroxidase-like and oxidase-like activities of MnIONPs, with the smaller particles exhibiting higher oxidative stress in vitro. However, MFH experiments demonstrated that cell toxicity is primarily influenced by the thermal effects associated with particle size, as the MnIONP_28 nm sample maintained temperatures above 42°C for almost the entire treatment, leading to significant cell death. This reinforces the critical role of temperature control in hyperthermia treatments and suggests that the thermal properties of nanoparticles outweigh their catalytic activity in determining treatment efficacy.

Overall, these findings emphasize the dual functionality of MnIONPs, combining size-dependent magnetic and catalytic properties, which can be leveraged for tailored oncological therapies. Future studies should explore the long-term biocompatibility and in vivo efficacy of these nanoparticles to further establish their clinical potential.

Author Contributions

M.R. and T.E.T. designed the research. E.L.J., E.L.W., and R.D.Z. supervised the research. M.A.M.O., M.R., T.E.T., M.V.M., E.L.J., and E.L.W. performed the experiments. E.L.W. and R.D.Z. provided new reagents and analytical tools. M.R. and T.E.T., with contributions from the other co-authors, performed data analysis and wrote the manuscript.

Acknowledgments

The authors thank the Argentinean ANPCyT for financial support through grants PICT 2018-02565, 2019-01859, 2019-02059, and PICT-BCIE 2021-00155. Thanks to the MSCA RISE-2020 101007629-NESTOR projects. Additionally, the authors thank the Fundación José A. Balseiro for funding the acquisition of the cell counter (project 2020). Dr. Torres and Dr. Raineri thank CONICET for the postdoctoral fellowship and the PIBAA-2023 grant, respectively. The authors also thank D.P. Valdés for reviewing the manuscript and providing valuable suggestions. The grammar and academic tone of the manuscript were enhanced with the assistance of ChatGPT 4.0.

Ethics Statement

The authors have nothing to report.

Consent

The authors have nothing to report.

Conflicts of Interest

The authors declare no conflicts of interest.

Data Availability Statement

All data supporting the findings of this study are included within the manuscript and Supporting Information. Additional datasets are available at the CONICET Research Data Repository. The datasets generated and/or analyzed during the current study are available at CONICET Research Data Repository.

References

1. H. Fatima and K.-S. Kim, "Magnetic Nanoparticles for Bioseparation," *Korean Journal of Chemical Engineering* 34 (2017): 589–599.

2. T. A. P. Rocha-Santos, "Sensors and Biosensors Based on Magnetic Nanoparticles," *TrAC, Trends in Analytical Chemistry* 62 (2014): 28–36.

3. Y. Miao, Q. Xie, H. Zhang, et al., "Composition-Tunable Ultrasmall Manganese Ferrite Nanoparticles: Insights Into Their in Vivo T1 Contrast Efficacy," *Theranostics* 9 (2019): 1764–1776.

4. J. Gallo, N. J. Long, and E. O. Aboagye, "Magnetic Nanoparticles as Contrast Agents in the Diagnosis and Treatment of Cancer," *Chemical Society Reviews* 42 (2013): 7816.

5. G. Goya, V. Grazu, and M. Ibarra, "Magnetic Nanoparticles for Cancer Therapy," *Current Nanoscience* 4 (2008): 1–16.

6. B. Thiesen and A. Jordan, "Clinical Applications of Magnetic Nanoparticles for Hyperthermia," *International Journal of Hyperthermia* 24 (2008): 467–474.

7. T. J. Carter, G. Agliardi, F. Lin, et al., "Potential of Magnetic Hyperthermia to Stimulate Localized Immune Activation," *Small* 17 (2021): 2005241.

8. N. A. Usov and B. Y. Liubimov, "Dynamics of Magnetic Nanoparticle in a Viscous Liquid: Application to Magnetic Nanoparticle Hyperthermia," *Journal of Applied Physics* 112 (2012): 023901.

9. J. Carrey, B. Mehdaoui, and M. Respaud, "Simple Models for Dynamic Hysteresis Loop Calculations of Magnetic Single-Domain Nanoparticles: Application to Magnetic Hyperthermia Optimization," *Journal of Applied Physics* 109 (2011): 083921.

10. B. Sanz, R. Cabreira-Gomes, T. E. Torres, et al., "Low-Dimensional Assemblies of Magnetic MnFe2O4 Nanoparticles and Direct in Vitro Measurements of Enhanced Heating Driven by Dipolar Interactions: Implications for Magnetic Hyperthermia," *ACS Applied Nano Materials* 3 (2020): 8719–8731.

11. E. Mazarío, J. Sánchez-Marcos, N. Menéndez, et al., "High Specific Absorption Rate and Transverse Relaxivity Effects in Manganese Ferrite Nanoparticles Obtained by an Electrochemical Route," *Journal of Physical Chemistry C* 119 (2015): 6828–6834.

12. J. Kim, H. Y. Kim, S. Y. Song, et al., "Synergistic Oxygen Generation and Reactive Oxygen Species Scavenging by Manganese Ferrite/Ceria co-Decorated Nanoparticles for Rheumatoid Arthritis Treatment," *ACS Nano* 13 (2019): 3206–3217.

13. J. Han and J. Yoon, "Supramolecular Nanozyme-Based Cancer Catalytic Therapy," *ACS Applied Bio Materials* 3 (2020): 7344–7351.

14. S. Yin, G. Song, Y. Yang, et al., "Persistent Regulation of Tumor Microenvironment via Circulating Catalysis of MnFe2O4@Metal–Organic Frameworks for Enhanced Photodynamic Therapy," *Advanced Functional Materials* 29 (2019): 1901417.

15. L. Gao, J. Zhuang, L. Nie, et al., "Intrinsic Peroxidase-Like Activity of Ferromagnetic Nanoparticles," *Nature Nanotechnology* 2 (2007): 577–583.

16. Y. Huang, J. Ren, and X. Qu, "Nanozymes: Classification, Catalytic Mechanisms, Activity Regulation, and Applications," *Chemical Reviews* 119 (2019): 4357–4412.

17. F. F. Peng, Y. Zhang, and N. Gu, "Size-Dependent Peroxidase-Like Catalytic Activity of Fe3O4 Nanoparticles," *Chinese Chemical Letters* 19 (2008): 730–733.

18. F. Ahmad, M. M. Salem-Bekhit, F. Khan, et al., "Unique Properties of Surface-Functionalized Nanoparticles for Bio-Application: Functionalization Mechanisms and Importance in Application," *Nanomaterials* 12 (2022): 1333.

19. F. Yu, Y. Huang, A. J. Cole, and V. C. Yang, "The Artificial Peroxidase Activity of Magnetic Iron Oxide Nanoparticles and Its Application to Glucose Detection," *Biomaterials* 30 (2009): 4716–4722.

20. B. Jiang, D. Duan, L. Gao, et al., "Standardized Assays for Determining the Catalytic Activity and Kinetics of Peroxidase-Like Nanozymes," *Nature Protocols* 13 (2018): 1506–1520.

21. M. Raineri, E. L. Winkler, T. E. Torres, et al., "Effects of Biological Buffer Solutions on the Peroxidase-Like Catalytic Activity of Fe3O4 Nanoparticles," *Nanoscale* 11 (2019): 18393–18406.

22. J. De Aguilar Diaz Leon and C. R. Borges, "Evaluation of Oxidative Stress in Biological Samples Using the Thiobarbituric Acid Reactive Substances Assay," *Journal of Visualized Experiments* 159 (2020): e61122.

23. Z. Ma, J. Mohapatra, K. Wei, J. P. Liu, and S. Sun, "Magnetic Nanoparticles: Synthesis, Anisotropy, and Applications," *Chemical Reviews* 123 (2023): 3904–3943.

24. A. G. Roca, L. Gutiérrez, H. Gavilán, M. E. Fortes Brollo, S. Veintemillas-Verdaguer, and M. d. P. Morales, "Design Strategies for Shape-Controlled Magnetic Iron Oxide Nanoparticles," *Advanced Drug Delivery Reviews* 138 (2019): 68–104.

25. Y. Hadadian, H. Masoomi, A. Dinari, et al., "From Low to High Saturation Magnetization in Magnetite Nanoparticles: The Crucial Role of the Molar Ratios Between the Chemicals," *ACS Omega* 7 (2022): 15996–16012.

26. C. W. Lai, F. W. Low, M. F. Tai, and S. B. Abdul Hamid, "Iron Oxide Nanoparticles Decorated Oleic Acid for High Colloidal Stability," *Advanced Polymer Technology* 37 (2018): 1712–1721.

27. E. De Biasi, E. Lima, C. A. Ramos, A. Butera, and R. D. Zysler, "Effect of Thermal Fluctuations in FMR Experiments in Uniaxial Magnetic Nanoparticles: Blocked vs. Superparamagnetic Regimes," *Journal of Magnetism and Magnetic Materials* 326 (2013): 138–146.

28. A. C. M. Maldonado, E. L. Winkler, M. Raineri, et al., "Free-Radical Formation by the Peroxidase-Like Catalytic Activity of MFe2O4 (M = Fe, Ni, and Mn) Nanoparticles," *Journal of Physical Chemistry C* 123 (2019): 20617–20627.

29. S. Bhattacharjee, "DLS and Zeta Potential – What They Are and What They Are Not?," *Journal of Controlled Release* 235 (2016): 337–351.

30. W. Aadinath and V. Muthuvijayan, "Influence of Oleic Acid Coating on the Magnetic Susceptibility and Fenton Reaction-Mediated ROS

Generation by the Iron Oxide Nanoparticles," *Nano Express* 5 (2024): 015017.

31. K. O'Grady and R. W. Chantrell, "Remanence Curves of Fine Particle Systems I: Experimental Studies," in *Magnetic Properties of Fine Particles* (Elsevier, 1992).

32. M. M. Cruz, L. P. Ferreira, A. F. Alves, et al., *Nanoparticles for Magnetic Hyperthermia*, ed. Grumezescu and Ficai (Elsevier, 2017), https://www.sciencedirect.com/science/article/abs/pii/B9780323461443000192?via%3Dihub.

33. V. R. R. Aquino, L. C. Figueiredo, J. A. H. Coaquira, M. H. Sousa, and A. F. Bakuzis, "Magnetic Interaction and Anisotropy Axes Arrangement in Nanoparticle Aggregates Can Enhance or Reduce the Effective Magnetic Anisotropy," *Journal of Magnetism and Magnetic Materials* 498 (2020): 166170.

34. A. J. Rondinone, C. Liu, and Z. J. Zhang, "Determination of Magnetic Anisotropy Distribution and Anisotropy Constant of Manganese Spinel Ferrite Nanoparticles," *Journal of Physical Chemistry B* 105 (2001): 7967–7971.

35. A. F. Bakuzis, P. C. Morais, and F. Pelegrini, "Surface and Exchange Anisotropy Fields in MnFe2O4 Nanoparticles: Size and Temperature Effects," *Journal of Applied Physics* 85 (1999): 7480–7482.

36. E. A. Périgo, G. Hemery, O. Sandre, et al., "Fundamentals and Advances in Magnetic Hyperthermia," *Applied Physics Reviews* 2 (2015): 041302.

37. E. Lima, E. De Biasi, M. V. Mansilla, et al., "Heat Generation in Agglomerated Ferrite Nanoparticles in an Alternating Magnetic Field," *Journal of Physics D: Applied Physics* 46 (2013): 045002.

38. L. C. Branquinho, M. S. Carrião, A. S. Costa, et al., "Effect of Magnetic Dipolar Interactions on Nanoparticle Heating Efficiency: Implications for Cancer Hyperthermia," *Scientific Reports* 3 (2013): 2887.

39. L. Gao, K. Fan, and X. Yan, "Iron Oxide Nanozyme: A Multifunctional Enzyme Mimetic for Biomedical Applications," *Theranostics* 7 (2017): 3207–3227.

40. B. Herrero de la Parte, I. Rodrigo, J. Gutiérrez-Basoa, et al., "Proposal of New Safety Limits for in Vivo Experiments of Magnetic Hyperthermia Antitumor Therapy," *Cancers* 14 (2022): 3084.

41. Z. Yan, A. Chaluvadi, S. FitzGerald, et al., "Effect of Manganese Substitution of Ferrite Nanoparticles on Particle Grain Structure," *Nanoscale Advances* 4 (2022): 3957–3965.

42. Q. Song, Y. Ding, Z. L. Wang, and Z. J. Zhang, "Tuning the Thermal Stability of Molecular Precursors for the Nonhydrolytic Synthesis of Magnetic MnFe2O4 Spinel Nanocrystals," *Chemistry of Materials* 19 (2007): 4633–4638.

43. K. Moghaddari, L. Schumacher, R. Pöttgen, and G. Kickelbick, "Optimizing Superparamagnetic Ferrite Nanoparticles: Microwave-Assisted vs. Thermal Decomposition Synthesis Methods," *Nanoscale Advances* 7 (2025): 4563–4576.

44. B. D. Cullity and C. D. Graham, *Introduction to Magnetic Materials*, 2nd ed. (Wiley, 2008).

45. R. C. C. Costa, M. De Fátima Fontes Lelis, L. C. A. Oliveira, et al., "Remarkable Effect of Co and Mn on the Activity of $Fe_{3-x}M_xO_4$ Promoted Oxidation of Organic Contaminants in Aqueous Medium With H2O2," *Catalysis Communications* 4 (2003): 525–529.

46. X. Liang, Z. He, Y. Zhong, et al., "The Effect of Transition Metal Substitution on the Catalytic Activity of Magnetite in Heterogeneous Fenton Reaction: In Interfacial View," *Colloids and Surfaces A: Physicochemical and Engineering Aspects* 435 (2013): 28–35.

47. Y. Peng, Z. Wang, W. Liu, et al., "Size- and Shape-Dependent Peroxidase-Like Catalytic Activity of MnFe2O4 Nanoparticles and Their Applications in Highly Efficient Colorimetric Detection of Target Cancer Cells," *Dalton Transactions* 44 (2015): 12871–12877.

48. A. A. de Almeida, E. De Biasi, M. V. Mansilla, et al., "Magnetic Hyperthermia Experiments With Magnetic Nanoparticles in Clarified Butter Oil and Paraffin: A Thermodynamic Analysis," *Journal of Physical Chemistry C* 124 (2020): 27709–27721.

49. X. Zhang, X. Mao, S. Li, W. Dong, and Y. Huang, "Tuning the Oxidase Mimics Activity of Manganese Oxides via Control of Their Growth Conditions for Highly Sensitive Detection of Glutathione," *Sensors and Actuators B: Chemical* 258 (2018): 80–87.

50. C. Ramankutty and S. Sugunan, "Surface Properties and Catalytic Activity of Ferrospinels of Nickel, Cobalt and Copper, Prepared by Soft Chemical Methods," *Applied Catalysis, A: General* 218 (2001): 39–51.

51. L. C. A. Oliveira, J. D. Fabris, R. R. V. A. Rios, W. N. Mussel, and R. M. Lago, "Fe3-xMnxO4 Catalysts: Phase Transformations and Carbon Monoxide Oxidation," *Applied Catalysis, A: General* 259 (2004): 253–259.

52. E. M. Knavel and C. L. Brace, "Tumor Ablation: Common Modalities and General Practices," *Techniques in Vascular and Interventional Radiology* 16 (2013): 192–200.

53. C. A. Juan, J. M. Pérez de la Lastra, F. J. Plou, and E. Pérez-Lebeña, "The Chemistry of Reactive Oxygen Species (ROS) Revisited: Outlining Their Role in Biological Macromolecules (DNA, Lipids and Proteins) and Induced Pathologies," *International Journal of Molecular Sciences* 22 (2021): 4642.

Supporting Information

Additional supporting information can be found online in the Supporting Information section. **Data S1.** Supporting Information.